RESEARCH ARTICLE

Key Points:
- We present lab observation of friction-stability-permeability evolution of a fracture in granite
- Two plausible mechanisms constraining friction-permeability relationship are proposed
- Results are fundamental in simulating hydraulic stimulation and seismic cycle

Correspondence to:
T. Ishibashi,
takuya.ishibashi@aist.go.jp

Friction-Stability-Permeability Evolution of a Fracture in Granite

Takuya Ishibashi[1] , Derek Elsworth[2] , Yi Fang[3] , Jacques Riviere[4,5] , Benjamin Madara[4] , Hiroshi Asanuma[1] , Noriaki Watanabe[6] , and Chris Marone[4]

[1]Fukushima Renewable Energy Institute, National Institute of Advanced Industrial Science and Technology, Koriyama, Japan, [2]Department of Energy and Mineral Engineering, EMS Energy Institute, and G3 Center, Pennsylvania State University, University Park, PA, USA, [3]Institute for Geophysics, Jackson School of Geoscience, University of Texas at Austin, Austin, TX, USA, [4]Department of Geosciences, Pennsylvania State University, University Park, PA, USA, [5]Now at Université Grenoble Alpes, ISTerre, Grenoble, France, [6]Department of Environmental Studies for Advanced Society, Graduate School of Environmental Studies, Tohoku University, Aoba-ku, Japan

Abstract The evolution of frictional strength, stability, and fracture permeability is intimately linked both to the seismic cycle and to the impact of hydraulic stimulation for fractured reservoirs. However, despite this importance, the poromechanical relationships between fault permeability and strength remain unclear. The present study explores this relationship via laboratory experiments for concurrent shear-flow on smooth fractures of Westerly granite. The novelty of these experiments is that the shear velocity is precisely controlled during the measurement of fracture permeability. Results indicate permeability enhancement during velocity-weakening (potentially unstable) frictional slip. To decipher key processes contributing to this response, we evaluate the state of contacting asperities and of fracture surface asperities via digital rock fracture modeling of statistically equivalent surfaces. We propose two plausible mechanisms constraining the relationship between friction and permeability evolution—one based on changes in asperity contact distribution and one on shear-induced dilation triggered by changes in fault slip velocity. These mechanisms should be taken into account in interpreting field observation such as the abrupt permeability increase of natural faults at the onset of seismic slip.

1. Introduction

Hydraulic stimulation of fractured reservoirs, such as geothermal and hydrocarbon reservoirs, is common practice in enhancing or maintaining the permeability of reservoirs (Evans et al., 2005; Häring et al., 2008). The injection of pressurized fluid into a reservoir may reactivate preexisting fractures in shearing mode with the opportunity for self-propping on asperities. The onset of fracture slip may be either seismic or aseismic (Ellsworth, 2013; Guglielmi et al., 2015; Lengliné et al., 2017), and thus, the evolution of crustal permeability may develop in either of these modes. Although a relation between mode of deformation (seismic versus aseismic) and permeability change is fundamental in defining the impact of hydraulic stimulation or for representing the nucleation of seismicity (McClure & Horne, 2012; Norbeck & Horne, 2016; Scuderi & Collettini, 2016), this relation has rarely been investigated and is generally poorly understood.

The evolution of frictional strength during fracture slip may be generally interpreted in the framework of rate- and state-dependent friction (Dieterich, 1978, 1979; Ruina, 1983), where the shear velocity, slip history (state of true contacts at the interface), and normal stress are the parameter variables. In this framework, the slip event may be fast/seismic or slow/aseismic depending on the friction constitutive properties (Marone, 1998) modulated via the elastic stiffness of the fracture and surrounding rock (Rice & Ruina, 1983). The rate- and state-frictional constitutive equation is commonly written as

$$\mu = \mu_0 + a \ln\left(\frac{v}{v_0}\right) + b \ln\left(\frac{v\theta}{D_c}\right) \tag{1}$$

where upon a velocity increase from v_0 to v (Figure 1a), the frictional coefficient (μ) increases from a reference steady state (μ_0), by an instantaneous so-called direct effect, and then evolves to a new steady state (evolution effect) over a characteristic critical slip distance (D_c; Figure 1b). θ is a state variable, which is generally
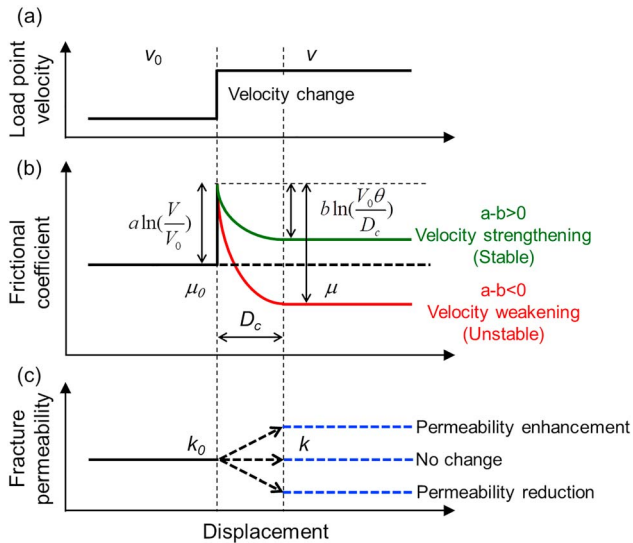
Figure 1. (a) Step change in the load point velocity during fracture shearing. (b) Idealized rate- and state-friction response to an increase in load point velocity. Two alternative behaviors (i.e., velocity strengthening and velocity weakening) are shown. (c) Predicted responses of fracture permeability to an increase in load point velocity.

interpreted as the average lifetime of frictional contacts and evolves with time and slip according to a state evolution law such as (Dieterich, 1979; Marone, 1998):

$$\frac{d\theta}{dt} = 1 - \frac{v\theta}{D_c} \qquad (2)$$

The parameters a and b in equation (1) are scaling factors that define the frictional stability. If friction increases with a velocity increase, the material is velocity-strengthening, leading to stable/aseismic slip (i.e., $(a - b) > 0$). Conversely, if ultimate friction decreases with a velocity increase, the material is velocity-weakening (i.e., $(a-b) < 0$), a necessary (though not sufficient) condition for stick-slip behavior associated with earthquake nucleation (i.e., potentially unstable slip; e.g., Marone, 1998, Scholz, 2002). Existing works show that the full spectrum of failure modes, ranging from earthquake rupture to aseismic slip, can be produced by specifying the ratio of the elastic loading stiffness to the frictional weakening rate (Leeman et al., 2016).

In contrast, it remains unclear how fracture permeability will evolve during slip and how permeability is linked to the mechanical characteristics of fracture. Fracture permeability may be enhanced during shear slip when the initial roughness of the fracture surfaces is large (Esaki et al., 1999). This roughness is manifest from asperities that may self-prop the fracture during shearing and result in connected pathways of new or enhanced porosity. Similar mechanisms have been explored via numerical modeling of fracture flow (Ishibashi, Watanabe, et al., 2016; Matsuki et al., 2006). Counter observations note decreases in fracture permeability/transmissibility with shearing when the initial geometries of the fracture surfaces are relatively smooth (Faoro et al., 2009; Giwelli et al., 2016). The destruction of asperities and the production of gouge material via wear are key factors in this evolution of fracture permeability. Of specific interest is whether the response of fracture permeability is linked to the frictional stability or not (Figure 1c). To explore such a link, fracture permeability may be monitored as an instantaneous step in shear velocity is applied, to implicitly link observations of frictional and permeability evolution.

The purpose of this paper is to explore such a relationship between the evolution of frictional strength, frictional stability (stable/unstable), and the response of fracture permeability. We describe laboratory experiments and results of numerical modeling to examine concurrent shear and flow along fractures in Westerly granite. The novelty of these experiments is that both upsteps and downsteps in shear velocity may be applied to supplement observations from prior experiments (Elkhoury et al., 2011; Faoro et al., 2009). Furthermore, we use models of evolving aperture distribution, coupled with distributed parameters models of fluid flow through the rock fracture, to follow the evolution of permeability—with aperture defined from fracture roughness recovered from optical profilometry. Such coupling between experimental observations and analysis is used to illuminate the relationship between fault strength, the stability of frictional sliding, and permeability.

2. Experimental Method

We conduct experiments to measure the evolution of friction, frictional stability, and the response of fracture permeability during shearing under stress. We use optical profiling to evaluate changes in fracture surface topographies during shearing and mechanistically link these observations to friction, stability, and permeability.

2.1. Rock Sample and Experimental Apparatus

The fracture slip experiments are conducted on L-shaped blocks of Westerly granite (Figure 2a) that include a precut fracture parallel to the shear direction. The fracture surfaces are preroughened with #60 grit (423 μm) silicon carbide to yield a controlled fracture roughness—verified by optical profilometry. Samples are loaded in a single direct-shear configuration within a pressure vessel and biaxial load frame (Figure 2) to create a true-triaxial stress state (for details of the apparatus, see Samuelson et al., 2009, and Candela et al., 2015).
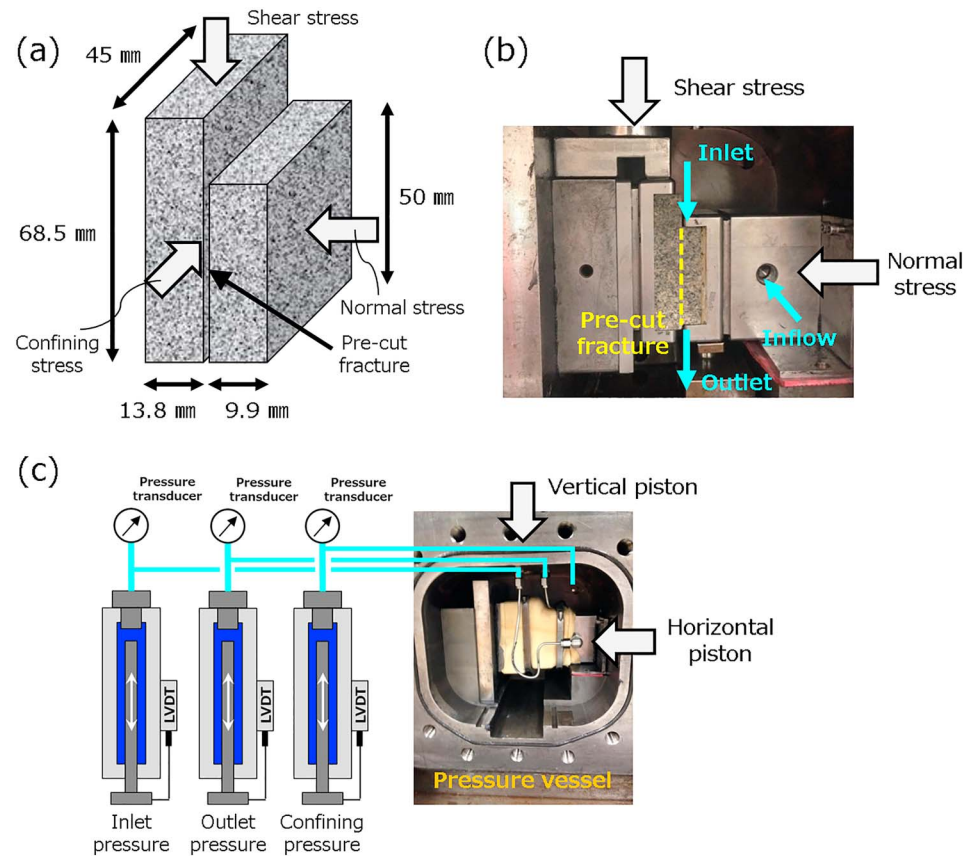
Figure 2. (a) L-shape block of Westerly granite with a single precut fracture. (b) Experimental configuration for measuring the frictional strength of a rock fracture. (c) Experimental configuration for measuring the permeability of a rock fracture.

The normal stress (σ_n) is applied on the fracture plane (45 mm × 50 mm; Figure 2) via a piston driven by a servo-controlled hydraulic ram and shear stress (τ) is applied by a separate, vertically oriented, piston driven by a servo-controlled hydraulic ram. The L-shaped block and forcing blocks/platens are unjacketed for measuring rock friction, alone (Figure 2b), but are jacketed (latex rubber sleeve) for measuring permeability (Figure 2c).

Normal and shear loads are measured by load cells with a resolution of 0.1 kN, and displacement of the vertical hydraulic ram is measured by displacement transducer mounted on the biaxial load frame with a resolution of 0.1 μm. Moreover, for flow-through experiments (i.e., permeability measurement for rock fractures), confining pressure (P_c), inlet pressure (P_{in}), and outlet pressure (P_{out}) are servo-controlled using fast-response hydraulic servo-controllers and measured by pressure transducers mounted at the pressure intensifiers with a resolution of 7 kPa, and both inlet and outlet flow volumes are measured using linear variable differential transformers set on the pressure intensifier pistons with a resolution of 5.1×10^{-5} cm³. When we measure fracture permeability, we confirm that inlet and outlet mass flow rates are within 1%. During permeability measurements of the respective velocity up/down-step stages, we hold the differential pore pressure (P_{in}-P_{out}) constant and monitor the change in flow rate so that the rock facture is constantly saturated by pore fluid. Measurements are taken continuously with a 24 bit analog to digital converter at 10 kHz and averaged to recording rates of 100 Hz. In the case of the fluid-flow-through experiments, fracture permeability is evaluated based on the cubic law (Tsang & Witherspoon, 1981; Witherspoon et al., 1980):

$$k = \frac{e_h^2}{12},$$ (3)

where k is the fracture permeability and e_h is the hydraulic aperture. Using Darcy's law, these parameters are related as

Table 1
Experimental Details and Evaluated Parameters

Experiment	Normal stress (MPa)	Confining pressure (MPa)	Differential pore pressure (kPa)	v_0 (μm/s)	v (μm/s)	μ_0 (−)	μ (−)	a-b (−)	k_0 (m²)	k (m²)	$(k$-$k_0)/k_0$	Figure number
p4502	6	0	0	1	3	0.806	0.804	−0.0018				Figure 4a
p4502	6	0	0	1	10	0.809	0.805	−0.0017	No permeability measurement			Figure 4a
p4502	6	0	0	1	20	0.809	0.807	−0.0007				Figure 4a
p4502	9	0	0	1	3	0.784	0.783	−0.0009				Figure 4b
p4502	9	0	0	1	10	0.786	0.781	−0.0022				Figure 4b
p4502	9	0	0	1	20	0.785	0.777	−0.0027				Figure 4b
p4503	12	0	0	1	3	0.860	0.858	−0.0018				Figure 4c
p4503	12	0	0	1	10	0.858	0.854	−0.0017				Figure 4c
p4503	12	0	0	1	20	0.859	0.854	−0.0017				Figure 4c
p4504	6	6	40	1	3		No friction measurement		8.14×10^{-11}	n.a.	n.a.	Figure 5a
p4504	6	6	40	1	10				n.a.	5.17×10^{-11}	n.a.	Figure 5a
p4504	6	6	40	1	20				4.02×10^{-11}	4.16×10^{-11}	0.033	Figure 5a
p4504	9	9	80–120	1	3				2.34×10^{-11}	2.21×10^{-11}	−0.055	Figure 5b
p4504	9	9	80–120	1	10				9.61×10^{-12}	1.32×10^{-11}	0.372	Figure 5b
p4504	9	9	80–120	1	20				6.49×10^{-12}	1.04×10^{-11}	0.607	Figure 5b
p4504	12	12	180–200	1	3				1.44×10^{-12}	n.a.	n.a.	Figure 5c
p4504	12	12	180–200	1	10				1.03×10^{-12}	1.53×10^{-12}	0.485	Figure 5c
p4504	12	12	180–200	1	20				1.11×10^{-12}	1.73×10^{-12}	0.556	Figure 5c

$$e_h = \left(-\frac{12\eta L Q}{W \Delta P} \right)^{1/3}, \tag{4}$$

where Q is the flow rate, ΔP is the differential pore pressure (P_{in}-P_{out}), η is the fluid viscosity (1.002×10^{-3} Pa·s at 20 °C for distilled water), L is the flow path length (50 mm), and W is the width of the fracture (45 mm). Since the matrix permeability of Westerly granite is between 10^{-19} and 10^{-21} m² (Morrow et al., 1986; Trimmer et al., 1980) and is many orders-of-magnitudes smaller than the fracture permeability, we assume that fluid flow occurs primarily through the fracture and that the host rock is functionally impermeable.

2.2. Experimental Procedure

We measure frictional strength (continuous experiments, p4502 and p4503) and fracture permeability (p4504) of the same rock fracture in two independent experiments. We run separate experiments to simplify the process of collecting high-quality friction and permeability data, and also so that second-order friction effects are recorded without the obfuscating influence of piston seals and the rubber jacket, necessary for the measurement of permeability. The details of experimental conditions are shown in Table 1.

In the measurements of frictional evolution (p4502 and p4503), both confining pressure and differential pore pressure are set to 0. Before the experiments, the surface of the fracture is saturated by distilled water. We conduct fracture shearing experiments at normal stresses of 6, 9, and 12 MPa, where we continuously monitor the evolution of friction ($\mu = \tau/\sigma_n$) during shearing. Note that these normal stresses are maintained constant via the aforementioned servo-hydraulic controllers. In each stage, we conduct a series of velocity stepping experiments to explore the evolution of frictional stability. Shear velocity is stepped from 1 (i.e., base shear velocity) to 3 μm/s, then stepped from 1 to 10 μm/s, and then stepped from 1 to 20 μm/s (Table 1).

In the measurement of fracture permeability evolution (p4504), we first apply a small normal stress across the fracture and a small confining pressure and fully saturate the rock fracture with distilled water. Since the granite fracture has a high-permeability ($\gtrsim 10^{-12}$ m²) and therefore a small entry pressure, the fracture is not vacuum-saturated before the flow test—as it achieves saturation without this. Then, both the normal stress and the confining pressure are increased to the target values of 6, 9, and 12 MPa, and these stresses are maintained constant during each stage. In this experimental configuration, confining pressure acts both parallel and normal to the fracture plane (Figure 2a)—thus, fracture-normal and fracture-parallel stresses are equivalent to the confining stress. This gives a uniform biaxial stress confining the fracture. Thus, the influences of the confining stress on asperity-breakage/gouge production are accounted for in the context of the true-triaxial stress state. Then, we conduct fracture shearing experiments in each stage, where we monitor the evolution of fracture permeability during shearing. Distilled water is used, and the differential pore pressure is set to constant values of 40, 100, and 200 kPa in the experiments with confining pressure of 6, 9, and 12 MPa respectively. Note that the absolute value of pore pressure within the fracture is 800 kPa higher than the differential pore pressure. Total shear displacement for each stress state is commonly ~4.2 mm. By setting low inlet pressures, we successfully seal the sample to prevent short circuiting along the edges of the sample (see Candela et al., 2015; Samuelson et al., 2009). In each stage, we again conduct a series of
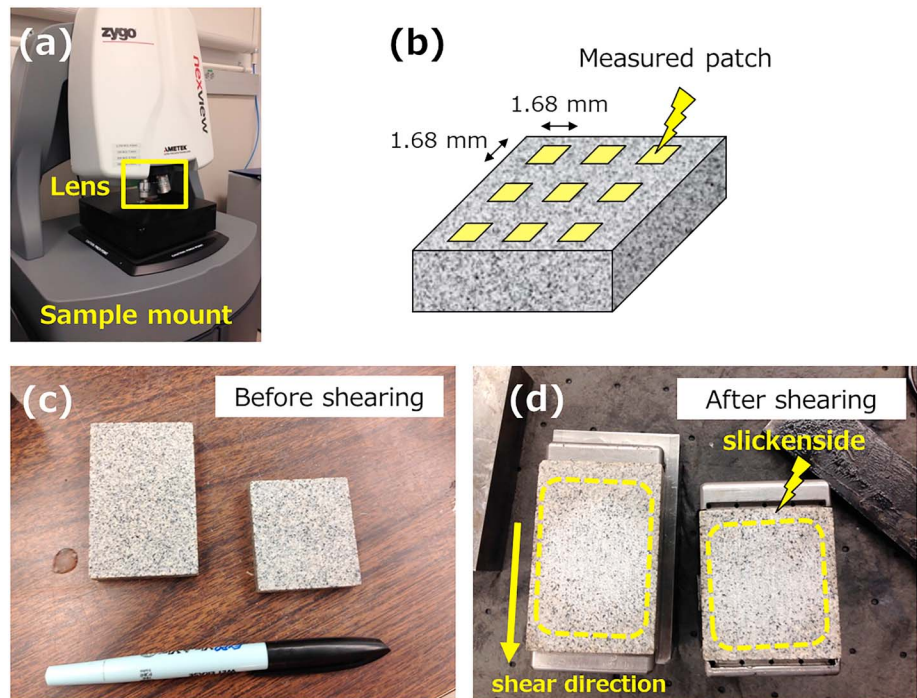
Figure 3. (a) The 3-D optical profilometer for characterizing roughness of fracture surfaces (ZYGO, NexView), (b) fracture surface for optical profiling, (c) fracture surfaces with no striations before fracture shearing, and (d) fracture surfaces with apparent striations after fracture shearing.

velocity stepping experiments. Shear velocity is stepped from 1 (i.e., base shear velocity) to 3 μm/s, then stepped from 1 to 10 μm/s, and then stepped from 1 to 20 μm/s (Table 1). The experiment is paused for the refilling of the fluid source reservoirs, due to the high permeability of the fracture (Ishibashi et al., 2015), but flow is maintained throughout the instant of the applied velocity step—to provide this unique observation.

2.3. Surface Profiling

To evaluate the change in fracture surface roughness caused by fracture shearing, measurements of fracture surface topography are conducted via a white light interferometer (ZYGO NexView, Figure 3a). This optical profilometer has a vertical resolution of 1 nm and a horizontal resolution of 1.642 μm over an area of 1.68 mm × 1.68 mm, defining a square grid 1,024 × 1024. Surface topography can be measured by optical profilometer in regions having a reflectance >1%. Considering that quartz (colorless mineral with very low reflectance) is one of the main components of granite, data loss in the quartz-rich regions (less than ~20% of the whole measured area) is inevitable in measuring the surface topography of granite. Thus, we do not directly use the measured topography data in the numerical modeling in section 4.1 as the sampling window covers only a small (but statistically complete) portion of the fracture. Rather, we use the measured statistical feature of roughness to generate both faces of the virtual fracture (Table 2).

For these evaluations, we conduct additional experiments on distilled-water-saturated Westerly granite fractures, which are roughened as noted in section 2.1. The fracture samples are sheared at normal stresses of 6 and 9 MPa at a velocity of 3 μm/s over a total shear displacement of ~6 mm. In these experiments, the confining pressure is set equivalent to the normal stress. Since these experiments are conducted only for the purpose of surface profiling, neither frictional strength nor fracture permeability of the fracture is measured.

Both before and after the fracture shearing experiment, we measure the surface topography at nine patches on each fracture surface (Figure 3b). Note that a rock fracture consists of two separated fracture surfaces (i.e., upper surface and lower surface). Root-mean-square (RMS), the vertical interval (interval between the peak and the valley lines for the data), and the fractal dimension are calculated for all sample windows and then

Table 2
Parameters for Characterizing Fracture Surface Topography

Normal stress (MPa)	Sample no.	Root mean square (mm)	σ_{RMS} (mm)	Vertical interval (mm)	σ_{VI} (mm)	Fractal dimension (−)
0 (No shear)	1	22.9	2.3	202	41.7	1.60
0 (No shear)	2	23.1	2.6	191	32.2	1.58
6	1	18.0	3.7	138	23.3	1.57
6	2	15.8	4.6	126	32.8	1.54
9	1	15.1	6.5	135	46.3	1.54
9	2	13.5	4.5	103	16.0	1.62

amalgamated as an ensemble for each fracture surface (Table 2). This is because we could not measure the same spot on fracture surface before and after shearing due to registration (fiducial) constraints. Figures 3c and 3d show typical views of the fracture surfaces both before and after fracture shearing, identifying the development of postshear striations (Figure 3d).

3. Experimental Results and Analysis

We examine the evolution of friction and permeability for the rock fracture under shear. In particular, we investigate the dynamic processes that alter the mechanical/hydraulic properties of fractures during shearing and their interaction.

### 3.1. Evolution in Frictional Coefficient During Fracture Shearing

Figure 4 shows the evolution of frictional coefficient (μ) during shearing (continuous experiments, p4502 and p4503), including the history of shear velocity (v). The frictional coefficient is near constant (~0.8) during the experiment and is in agreement with previous studies (e.g., Blanpied et al., 1998, Kilgore et al., 1993). Note that the slight change in the frictional coefficient depends on normal stress and may be due to a small change in the fracture inclination after a series of experiments (after regrinding the fracture surfaces).

In velocity-stepping experiments (Figure 4) we observe the classical evolution of rate state friction, which includes both the direct effect (abrupt increase in friction) and evolution effect (gradual decrease in friction), for individual velocity steps (Dieterich, 1978, 1979; Ruina, 1983). Thus, we evaluate frictional stability by calculating the friction rate parameter (a-b):

$$a - b = \frac{\mu - \mu_0}{\mathrm{1n}(v/v_0)} \tag{5}$$

where μ_0 and μ are the steady state coefficients of friction for sliding at velocities of v_0 and v. As shown in Figure 4d, both μ_0 and μ are determined from the average value of friction over the shear-displacement window ±0.05 mm, which accounts for noise and natural variability due to fault roughness and rock heterogeneity. We determine a statistical average for friction in a manner consistent with the definition of D_c (Figure 4d) as the critical slip distance required to achieve the steady state after the velocity step. In Figure 4, we find that a slip distance of ~100 μm is required to achieve the steady state friction after a velocity step. Based on this observation, D_c is estimated to be 100 μm. Considering that roughness is typically on the order of several tens of micrometers to hundreds of micrometers, the scale of D_c potentially relates to the microscale roughness of the fracture surface. Equation (5) defines the friction rate parameter (a-b), with positive values indicating velocity-strengthening behavior (i.e., stable/aseismic slip) and negative values indicating velocity-weakening, a necessary (but not sufficient) condition for stick-slip behavior associated with earthquake nucleation (i.e., potentially unstable slip; e.g., Marone, 1998, Scholz, 2002). In calculating the (a-b), we use the steady state, average value of friction. In other words, we do not perform fitting for the relation between friction and displacement with rate and state friction, nor do we consider transient oscillations on the friction data.

Table 1 summarizes friction rate parameter values for experiments p4502 and p4503, and data are plotted in Figure 6a as a function of velocity step size (ln(v/v_0)). Figure 6a indicates that (a-b) increases with an increase in the velocity step size at a normal stress of 6 MPa, whereas (a-b) decreases with an increase in the velocity
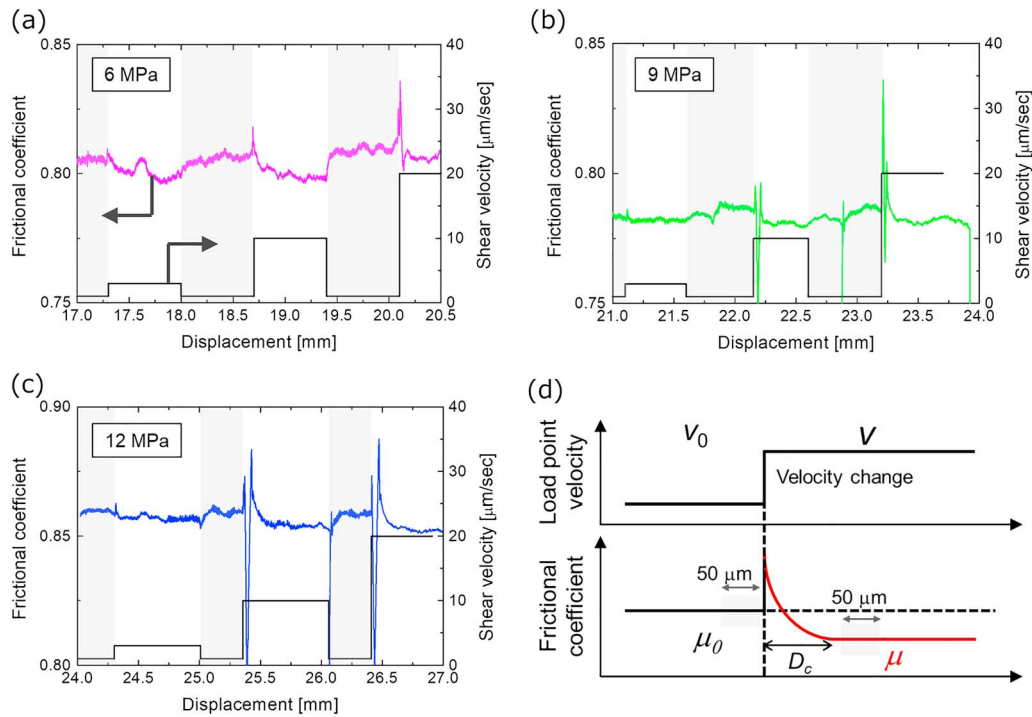
Figure 4. Experimental result showing frictional coefficient and shear velocity versus shear displacement at normal stresses of (a) 6, (b) 9, and (c) 12 MPa. Responses in the frictional coefficient caused by the shear velocity jump are analyzed.

step size at a normal stress of 9 MPa. At a normal stress of 12 MPa, there is no significant change in (*a-b*) with the velocity step size. Based on the experimental results, in this low normal stress range, we conclude that there is no dependency of (*a-b*) on velocity step size. Indeed, a dependency of (*a-b*) on temperature/humidity or on the percentage of clay and organic content is apparent (Blanpied et al., 1995; Fang et al., 2017; Frye & Marone, 2002; Kohli and Zoback, 2013), but dependency of (*a-b*) on velocity step size is not discussed in detail. Regardless of the normal stress or the velocity step size, the friction rate parameter (*a-b*) is uniformly negative, ranging from -0.0027 to -0.0009 (Figure 6a). These results are consistent with previous studies (Blanpied et al., 1987).

Subsequently, we discuss the influence of the confining stress on the friction rate parameter in exploring the links between frictional stability and permeability change in section 3.3. Marone et al. (1990) measured the (*a-b*) values for bare surfaces of Westerly granite within the triaxial pressure vessel (confined condition), and Kilgore et al. (1993) measured the (*a-b*) values for the same material in the moment-compensated double-direct shear apparatus (no confining stress condition). Both above cases reported negative (*a-b*) values, suggesting that the confining stress, as an individual potential influencing factor, does not change the (*a-b*) values from negative to positive.

In summary, experimental results reveal that the frictional shearing of Westerly granite is characterized by velocity-weakening behavior (potentially unstable slip), and such a characteristic will be preserved in the case that the confining pressure increases.

3.2. Evolution in Fracture Permeability During Fracture Shearing

Figure 5 shows the evolution of fracture permeability (*k*; p4504) for the history of shear velocity (*v*). Fracture permeability decreases with increasing normal stress (from 6 to 12 MPa), which is caused by the normal closure of the fracture due to the elastic deformations or the damage/crack at the contacting asperities (Chen et al., 2000; Jaeger et al., 2007; Kang et al., 2016; Pyrak-Nolte & Nolte, 2016). For these normal stress conditions, fracture permeability also decreases with increasing shear displacement. These reductions in *k* are due to the change in fracture roughness and the production of wear materials (Fang et al., 2017; Faoro
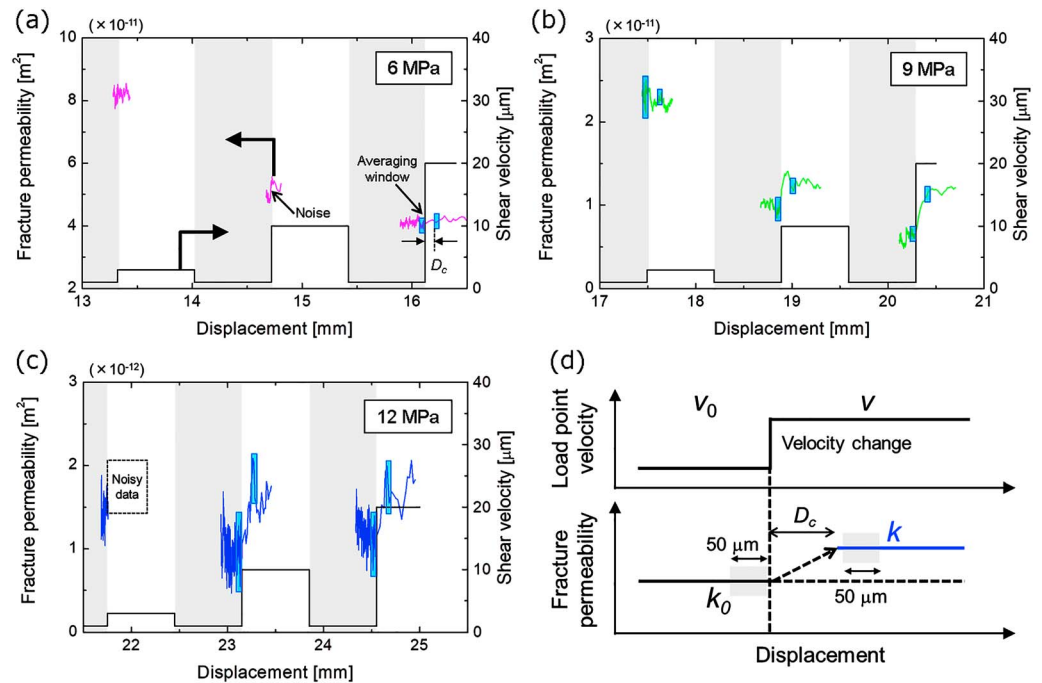
Figure 5. Experimental results showing fracture permeability and shear velocity versus shear displacement at normal stresses of (a) 6, (b) 9, and (c) 12 MPa. In each stage, confining stress is set equivalent to the normal stress (i.e., anisotropic stress condition). Responses in the fracture permeability caused by the shear velocity jump are analyzed.

et al., 2009; Wang & Scholz, 1994). In this study, the production of wear materials is not analyzed—but the source of these products—the change in fracture roughness—is quantitatively explored (see section 3.3).

In this experiment (p4504), we evaluate changes in fracture permeability due to instantaneous steps in shear velocity and explore the links between frictional stability and permeability change. The responses in k for various combinations of normal stress and velocity step size are shown in Figure 5. To highlight the essential trend in permeability change and ensure the reproducibility in the following analysis, the permeability data are filtered (e.g., Butterworth filter) and averaged to the recording rates of 10 Hz in Figure 5. Furthermore, to quantify the permeability change (Δk), we evaluate the fracture permeability both before (k_0) and then after (k) the instantaneous step in shear velocity. Measured permeabilities appear to fluctuate slightly, especially at a normal stress of 12 MPa (Figure 5c). This may be because the mechanical/hydraulic apertures before the velocity step are so small that the clogging/removal of wear materials at pore spaces significantly influences the connectivity of the flow paths. However, both k_0 and k are derived as the ensemble average of fracture permeabilities over the shear-displacement window ±0.05 mm (see Figure 5d); therefore, the impacts of permeability fluctuation on the evaluation of k_0 and k are minor. Also, when evaluating the (a-b) values (see section 3.1), D_c in Figure 5d is the critical slip distance required to achieve steady state friction after the velocity step, and transient behaviors from k_0 to k are not analyzed in detail. On the basis of results for frictional measurements (p4502 and p4503), D_c is set to 100 μm. This method for choosing the widow over which the permeability is averaged is systematic and rational—as based on the critical slip distance. The normalized permeability change is then defined as

$$\frac{\Delta k}{k_0} = \frac{k - k_0}{k_0}.$$

(6)

Because the shear-displacement window for defining $\Delta k/k_0$ is sufficiently small (less than ~0.2 mm; see Figure 5d), the background reduction in k with increasing shear displacement has little influence on the calculation of $\Delta k/k_0$. Considering that the fracture permeabilities after the velocity step are mostly higher than those before the velocity step (Figure 5), it is clear that fracture permeability is enhanced due to the velocity step. Such response in fracture permeability to the velocity step is preliminarily confirmed in Ishibashi,
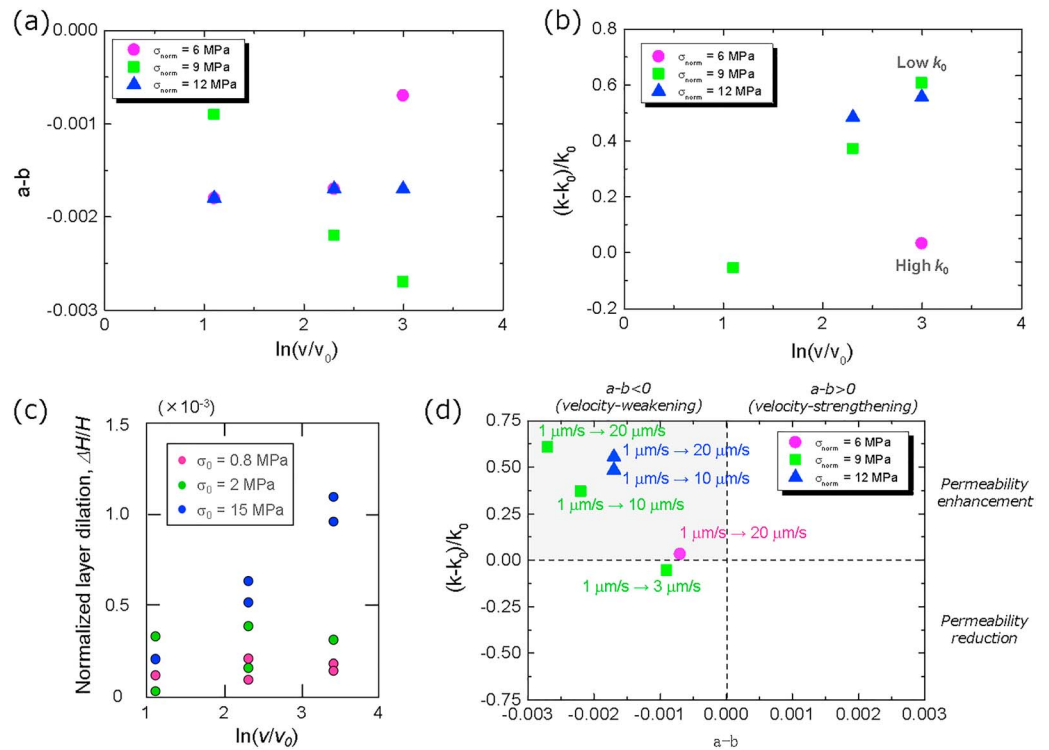
Figure 6. (a) Relationship between stability parameter (i.e., *a-b*) and velocity step size. (b) Relationship between normalized permeability change (i.e., $(k-k_0)/k_0$) and velocity step size. (c) Relationship between normalized dilation of a layer of quartz gouge and velocity step size (modified from Samuelson et al., 2009). (d) Relationship between the instability parameter and normalized permeability change.

Asanuma, et al. (2016) and is consistent with the experimental observation in Fang et al. (2018). Moreover, Im et al. (2018) has reported that permeability response switches from net reduction to net increase following fracture reactivation (i.e., upon reactivating an instantaneous slide following holding) that is consistent with the present study.

The normalized permeability changes ($\Delta k/k_0$) evaluated in experiment (p4504) are summarized in Table 1, and $\Delta k/k_0$ is also shown in Figure 6b as a function of velocity step size ($\ln(v/v_0)$). Note that $\Delta k/k_0$ is not evaluated when the original data include noise/uncertainty or the aforementioned window for ensemble averaging the permeability cannot be placed. The values of $\Delta k/k_0$ are quite small (<0.05) at a normal stress of 6 MPa, and $\Delta k/k_0$ increases with an increase in $\ln(v/v_0)$ at normal stresses of 9 and 12 MPa. The $\Delta k/k_0$ ranges from -0.055 to 0.607 in the experiments. In Figure 6b, larger values of $\Delta k/k_0$ are recorded when k_0 is small and that $\Delta k/k_0$ increases with velocity step size. These trends suggest that fracture dilation increases with velocity step size and agreeing with observations in velocity stepping experiments with fine-grained quartz fault gouge (Samuelson et al., 2009; Figure 6c).

Finally, based on the experimental results (p4502, p4503, and p4504), $\Delta k/k_0$ is shown as a function of the friction rate parameters (*a-b*) in Figure 6d. Although the experimental conditions differ slightly between frictional measurements (no confining stress) and permeability measurement (confined), these results are comparable. This is because the influence of confining stress, being applied both parallel to the fracture surface and perpendicular to the sliding direction, has negligible influence on the frictional stability. Figure 6c reveals that almost all points appear exclusively in the second quadrant of the graph, and this region represents both negative values of (*a-b*) and positive values of $\Delta k/k_0$. This suggests that the permeability enhancement of rock fractures is possibly created by the shearing of a fracture with velocity-weakening (potentially unstable slip) properties. This is consistent with field observations where fault permeability increases during seismic slip (Guglielmi et al., 2015), and this phenomenon may be related to the mechanisms of permeability enhancement of fracture zones excited by far-field earthquakes (Elkhoury et al., 2006; Xue et al., 2013).
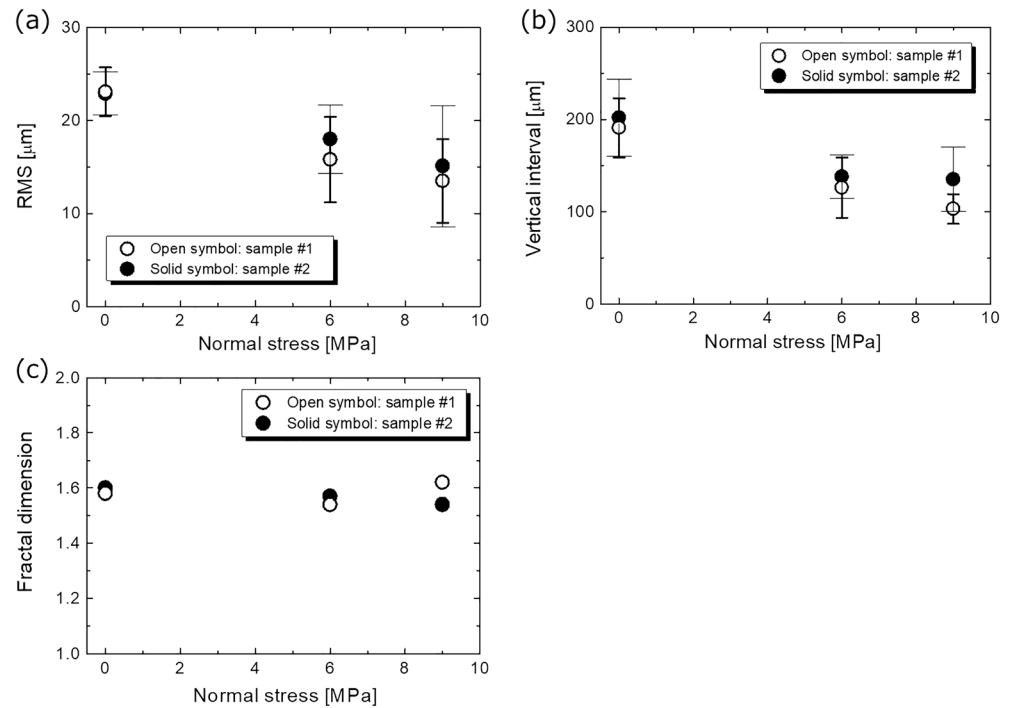
Figure 7. Changes in (a) root mean square (RMS), (b) vertical interval, and (c) fractal dimension for the fracture surfaces of Westerly granite with normal stress during fracture shearing.

3.3. Change in Surface Roughness Due to Fracture Shearing

Roughness characteristics of fracture surface topographies are obtained through surface measurements via white light interferometry (Table 2). These parameters are summarized in Figure 7 as a function of the normal stress (σ_n) applied during the experiment. In Figure 8, mean values for the respective parameters are plotted with their standard deviations. The decreases in the RMS and the vertical interval with increasing σ_n (Figures 7a and 7b) demonstrate that the surface becomes smoother (i.e., roughness is reduced) for experiments at high σ_n. Figure 7c reveals that the fractal dimension is nearly constant at ~1.58 regardless of σ_n. This result indicates that the complexity of the surface roughness is unchanged before and after fracture shearing.

Reductions in the RMS and the vertical interval result from breakage and crushing of the fracture surfaces during shear (Wang & Scholz, 1994). Considering that the fracture asperities play a significant role in maintaining the void space within fractures (Ishibashi, Watanabe, et al., 2016; Jaeger et al., 2007), the destruction of these asperities will likely reduce the fracture permeability. Some of the wear products will likely further reduce permeability by flow occlusion (Faoro et al., 2009; Giwelli et al., 2016), though the production of wear products is not quantified. The ratio of flushed materials to the total amount of detached materials is expected to be small since the pressure gradients are low for the fluid flow experiments (0.8 to 4 kPa/mm). On the other hand, only small changes in fractal dimension suggest that some geometrical characteristics of the surface roughness are maintained. Based on Scholz (1987), the thickness of wear is estimated to be 3 μm when the granite fracture is sheared over a total shear displacement of 20 mm at 12 MPa. The mechanism for enhancing the fracture permeability is discussed in section 4.3.

4. Interpretation and Discussion

We evaluate the evolution of mechanical/hydraulic properties and surface topographies of granite fractures during shearing. Experimental results identify that (1) the friction rate parameter (a-b) is uniformly negative, identifying velocity-weakening behavior; (2) the normalized permeability change ($\Delta k/k_0$) is generally positive, linking unstable slip to fracture permeability enhancement; and (3) the fractal characteristic of the rock
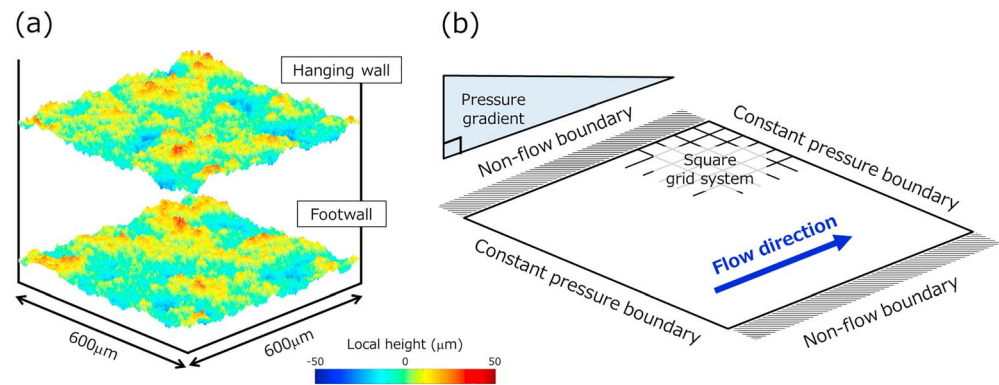
Figure 8. (a) Numerical modeling of fracture surfaces for determining fracture aperture distributions and (b) boundary conditions for unidirectional fluid flow simulation for the fracture aperture distribution created in a 1-μm square grid system.

fracture surfaces is consistently maintained both before and after fracture-shearing. Note that result (3) suggests that a steady state surface roughness is difficult to achieve. This result is consistent with a conceptual model of surface roughness evolution (Power et al., 1988), where newly produced wear products alter the initial surface irregularity and creates a new mismatch between the contacting surfaces.

In exploring the poromechanical relationships between mechanical and hydraulic properties of the rock fracture during shearing, we focus on the state of fracture surface roughness and contacting asperities. As in situ measurements of these properties (Kaproth & Marone, 2013; Renard et al., 2018) are difficult to determine, in the present study, we explore the state of fracture surface roughness and contacting asperities by using statistically equivalent digital rock fractures. In the digital rock fracture modeling, the fracture surface topography can be generated based on the self-affine nature of the fractal surfaces (Brown et al., 1995; Ishibashi et al., 2015; Kumar & Bodvarsson, 1990; Matsuki et al., 2006). The fractal nature of such surfaces seems valid for natural fault roughness over multiple length scales (Renard et al., 2013). Then, the aperture distribution of the rock fracture is determined by mating two self-affine fracture surfaces. The details of the digital rock fracture modeling method are introduced as follows.

4.1. Numerical Modeling of Fracture Aperture Distributions and Resulting Fluid Flow

The surface geometries of rock fractures are numerically modeled by a spectral method based on fractional Brownian motion (Peitgen & Saupe, 1988). In this method, a fractal surface is generated by the inverse Fourier transform of the Fourier components that are given according to the scaling law of the surface height determined by the fractal dimension of the rock surface. The method for generating fracture surfaces is consistent with that of Matsuki et al. (2006) or Ishibashi et al. (2015).

We model the fracture surface topographies using the measured roughness parameters, D and RMS (Table 2). Since these parameters vary in reflecting the normal stress (σ_n) applied during the fracture shearing and the generation of the resulting wear, the associated aperture distributions also vary depending on σ_n. As shown in Figure 8a, the distributions of contacting asperities/void space (hereinafter called *aperture distribution*) for the rock fracture consist of a pair of fracture surfaces (i.e., footwall and hanging wall). Since the footwall and hanging wall fracture surfaces are roughened by abrasive compound independently, the matedness between these two surfaces is much smaller than artificially created Mode I fracture (Matsuki et al., 2006). Note that the matedness is defined as how well-matched opposite fracture surfaces are (Barton et al., 1985; Olsson & Barton, 2001). Thus, in determining contact/void distributions of the rock fracture in the present study, we do not consider such concepts for the surface matedness and we contact a pair of numerically created fracture surfaces, which are uncorrelated.

The parameter values of Table 2 are used to define the surface topographies of square fractures numerically created at 1-μm spacing on a 600 μm × 600 μm grid. Six surface topographies are created, which are statistically equivalent but uncorrelated with each other (i.e., low matedness), for all σ_n values (e.g., 0, 6, and 9 MPa). By choosing two of these six surface topographies, we subsequently model the initial aperture distributions

with a single contact point, with the aperture distributions corresponding to those in the unloaded condition. Nine initial aperture distributions result for each condition of σ_n, yielding a total of 27 for the initial model. In this study, we treat the true contact-area ratio (R_c), which is defined as the ratio of the number of contacting points to the total number of grid elements, as a fitting parameter, since the value of R_c cannot be constrained merely from the experimental results. It should be noted that identifying the value of R_c of the real fracture requires in situ measurements via acoustoelastic measurements or via μ-focus X-ray computerized tomography (e.g., Fang et al., 2017; Kaproth & Marone, 2013).

For the respective initial models for the aperture distribution, we vary the value of R_c from 0 to 0.3 by decreasing the gap between the two opposing fracture surfaces. As a result, the aperture distribution of the rock fracture is also varied. The overlapping asperities, which evolve during fracture closure, are treated as contacting asperities (i.e., regions of zero aperture). The resulting deformations at contacting asperities are not considered herein (Jaeger et al., 2007). To estimate their hydraulic characteristics, such as fracture permeabilities or flow paths, we further simulate 2-D fluid flow at steady state by solving the Reynolds lubrication equation (Brown, 1987; Brush & Thomson, 2003; Ge, 1997):

$$\frac{\partial}{\partial x}\left(e^3 \frac{\partial P}{\partial x}\right) + \frac{\partial}{\partial y}\left(e^3 \frac{\partial P}{\partial y}\right) = 0, \tag{7}$$

where e is the aperture and P is the pressure of the fluid. The Reynolds equation is solved with a finite difference method under the boundary conditions of Figure 8b. Note that this condition honors the boundary conditions for the fluid flow experiment (p4504). The total flow rate, Q, is calculated from equation (7), and we then evaluate the fracture permeabilities by using equations (3) and (4). As the change in surface topographies or the change in flow paths during fracture shearing is not rigorously considered, this model is not a coupled hydromechanical approach. Note that the model used in our study only focuses on the most plausible link between contact area and fracture permeability and cannot treat the other possible mechanisms such as flux-driven unclogging.

### 4.2. Relations Between Contact Area and Fracture Permeability

We explore the relations between the true contact-area ratio, R_c ($0 < R_c < 1$), and the fracture permeability, k (m^2). Note that there is no contact when R_c is equal to 0 and there is no void space when R_c is equal to unity. Figures 9a–9c show the simulation results of R_c-k relation for different normal stresses (σ_n) applied during the experiment. The fracture surface topographies, as used for generating fracture aperture distributions, are varied depending on σ_n. In Figure 9, the symbols of plots are varied depending on the initial aperture distribution. Regardless of σ_n, the overall trend is for k to decline with increasing R_c, though k is not uniquely determined by R_c. As explained later, the upper/lower limits for the R_c-k relations are estimated from the red solid symbols in Figure 9.

Such variations in k are likely, due to the heterogeneous distributions in aperture and flow rate (Ishibashi et al., 2015; Watanabe et al., 2009) and due to the variations in mean aperture. To explain this mechanism, representative results for aperture distributions (color scale, left) and flow rate distributions (grey scale, right), corresponding to the marked plots in Figure 9c, are shown in Figure 10. In Figure 10, the contacting asperities are shown in black, and the flow rates are normalized to the maximum value of the flow rate. Parameter values characterizing the heterogeneous distributions in aperture and flow rate in Figure 10 are then summarized in Table 3. Regardless of aperture distributions, the flow area within the fracture is limited to between 28% and 39% of the whole fracture area. Aperture distributions in Figures 10a and 10c are characterized by approximately the same magnitude of fracture permeability ($k = 6.8 \times 10^{-12}$ m^2), although their true contact-area ratios and mean apertures are different ($R_c = 0.138$ and $e_m = 15.3$ μm for Figure 10a, whereas $R_c = 0.181$ and $e_m = 12.7$ μm for Figure 10c). Note that both e_m and e_h are evaluated on a selected region of the 600 μm × 600 μm window. Then the ratio of hydraulic aperture to mean aperture (e_h/e_m) is calculated to explore the tortuosity of the flow paths. Flow path tortuosity generally increases with a decrease in the parameter, e_h/e_m ($0 < e_h/e_m < 1$; Matsuki et al., 2006). The values of e_h/e_m are 0.60 for Figure 10a and 0.71 for Figure 10c—suggesting that the flow paths of Figure 10a are more tortuous. In contrast, the aperture distributions of Figures 10c and 10d are characterized by the same contact-area ratios ($R_c = 0.18$), although the fracture permeability in Figure 10d ($k = 1.1 \times 10^{-11}$ m^2) is ~1.6 times higher than the fracture permeability in
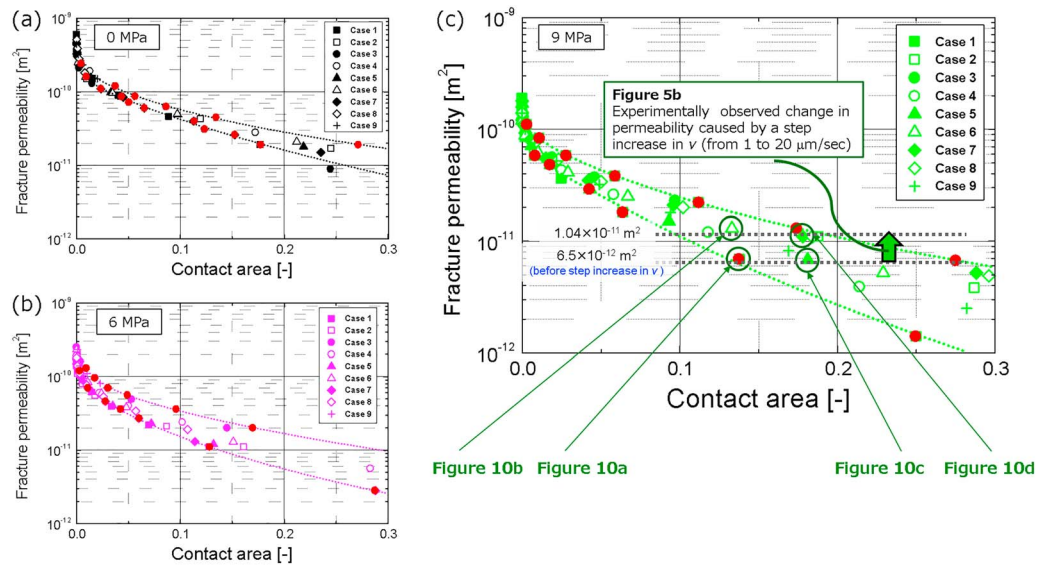
Figure 9. Changes in fracture permeability with the contact area at normal stresses of (a) 0, (b) 6, and (c) 9 MPa.

Figure 10c ($k = 6.8 \times 10^{-12}$ m^2). The values of e_h/e_m are 0.71 for Figure 10c and 0.81 for Figure 10d, thus suggesting that the flow paths of Figure 10c are more tortuous than those in Figure 10d. Our results are consistent with Heap and Kennedy (2016), where they note out that fracture permeability decreases with an increase in fracture tortuosity.
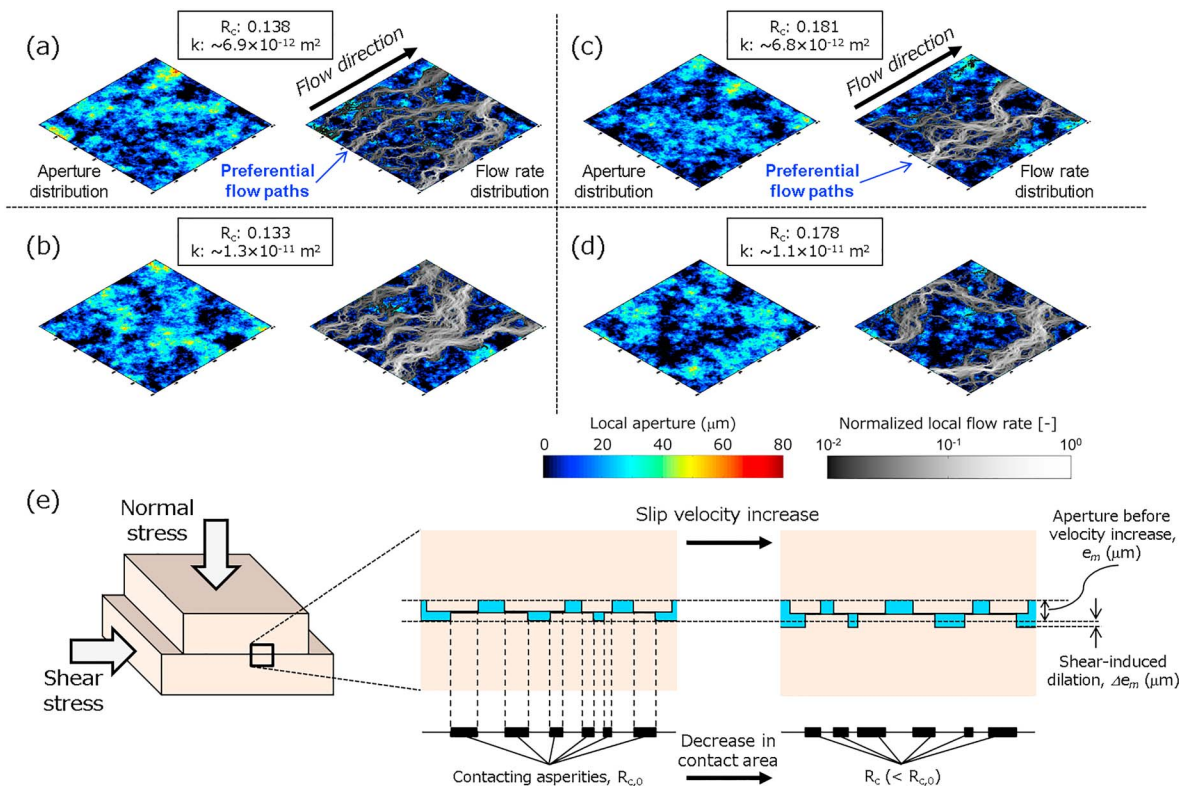
Figure 10. (a–d) Representative results for the aperture distributions and the local flow rate distributions within the numerically modeled fractures, which are marked in Figure 9c. (e) Schematic illustration of contacting asperities and of shear-induced dilation.

Table 3
Parameters for Characterizing the Aperture Distributions of Numerically Modeled Fractures

Figure number	Arithmetic mean aperture, e_m (mm)	Geometric mean aperture (mm)	Contact area (%)	Fracture permeability, k (m^2)	Hydraulic aperture, e_h (mm)	Flow area (%)	e_h/e_m
Figure 10a	15.3	13.3	13.8	6.9×10^{-12}	9.1	38	0.60
Figure 10b	15.9	14.1	13.3	1.3×10^{-11}	12.4	39	0.78
Figure 10c	12.7	11.6	18.1	6.8×10^{-12}	9	28	0.71
Figure 10d	14.2	13	17.8	1.1×10^{-11}	11.5	32	0.81

To quantify the R_c-k relationships, two envelopes corresponding to the upper/lower limits for the R_c-k relations bound the data of Figures 9a–9c. These enveloping curves for upper/lower limits are fitted by the following equation:

$$k = 10^{\left\{ \alpha \cdot (Log_{10}R_c)^3 + \beta \cdot (Log_{10}R_c)^2 + \gamma \cdot (Log_{10}R_c) + \delta \right\}}, \tag{8}$$

where α, β, γ, and δ are fitting parameters to constrain the relations. These parameter values for the individual enveloping curves are calculated based on the data shown with red solid symbols in Figure 9 and are summarized in Table 4. Considering the parameter values of e_h/e_m and mean aperture for the respective points in Figure 9, we conclude that the enveloping curves for the upper limits correspond to the large e_h/e_m (i.e., non-tortuous flow channels) and the large mean aperture, whereas the enveloping curves for lower limits correspond to the small e_h/e_m (i.e., tortuous flow channels) and small mean aperture. Regardless of σ_n, the variation in k for specific R_c is broad in the case of large R_c, since the number of variations in aperture distributions possibly increases with increasing R_c. Moreover, the variation in k for specific R_c becomes broad as the fracture surface roughness becomes smoother with elevated σ_n. Our suggested R_c-k relations are useful to decipher key processes that link mechanical and hydraulic properties of the rock fracture during shearing.

4.3. Linking Mechanical and Hydraulic Properties of Rock Fractures During Shearing

We explore the mechanisms that dictate the relationship between friction and permeability evolution during fracture shear.

We first focus on the specific experimental result, where shear velocity (v) is stepped from 1 to 20 μm/s at a normal stress of 9 MPa. Frictional coefficient is reduced from $\mu_0 = 0.785$ to $\mu = 0.777$ (i.e., velocity-weakening behavior), whereas fracture permeability is enhanced from $k_0 = 6.5 \times 10^{-12}$ m^2 to $k = 1.04 \times 10^{-11}$ m^2. To decipher the mechanisms constraining this response, the state of the contacting asperities is evaluated via digital rock fracture modeling (i.e., R_c-k relation) and is coupled with the experimental observations. Considering the framework of rate- and state-dependent friction (e.g., equation (1)), total shear force (F), is commonly described as

$$F = s(v) \cdot R_c(\theta), \tag{9}$$

where s is the average shear strength of the contacting asperities and R_c is the true contact-area ratio ($0 < R_c < 1$; Baumberger et al., 1999). The shear strength has a dependency on the shear velocity (v) and R_c varies in accordance with the slip history (state θ). $R_c(\theta)$ and $s(v)$ are furthermore written as

Table 4
Fitting Parameters for Constraining Relations Between Contact Area and Fracture Permeability

Normal stress (MPa)	Type of envelop	α	β	γ	δ
0 (No shear)	Upper limit	−0.11	−0.80	−2.13	−11.69
0 (No shear)	Lower limit	−0.37	−2.02	−3.99	−12.73
6	Upper limit	−0.25	−1.26	−2.63	−12.08
6	Lower limit	−0.22	−1.40	−3.37	−13.00
9	Upper limit	−0.17	−1.12	−2.71	−12.37
9	Lower limit	−0.51	−2.93	−5.89	−14.43
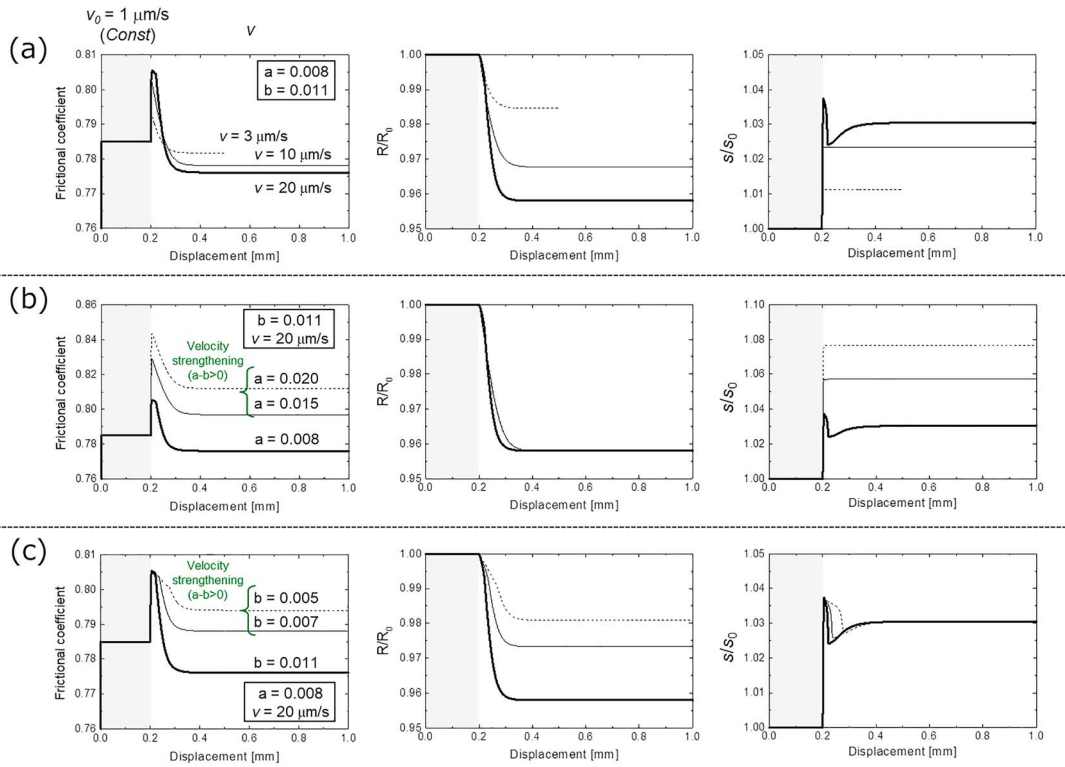
Figure 11. Parametric analysis for the evolution of frictional coefficient (μ), true contact-area ($R_c/R_{c,0}$), and shear strength (s/s_0): (a) effect of velocity step, (b) effect of *a* value, which relates to the direct effect, and (c) effect of *b* value, which relates to the evolution effect.

$$R_c(\theta) = R_{c,0}\left[1 + B\ln\left(\frac{\theta v_0}{D_c}\right)\right], \tag{10}$$

$$s(v) = s_0\left[1 + A\ln\left(\frac{v}{v_0}\right)\right], \tag{11}$$

where $R_{c,0}$, s_0, and v_0 are the initial values for the true-contact area ratio, shear strength, and shear velocity; D_c is a so-called critical slip distance; θ is a state variable (e.g., equation (2)); and A and B are the scaling parameters that relate to the *direct effect* and the *evolution effect*." Note that A and B are calculated as a/μ_0 and b/μ_0 by using the parameter values, a and b, in equation (1). In equations (10) and (11), the values of v_0, D_c, A, and B are given on the basis of the aforementioned experiment ($v_0 = 1$ μm/s, $D_c = \sim 100$ μm, $A = 0.01$, and $B = 0.014$). The time-dependent θ is calculated by coupling two equations; one is the state evolution law (equation (2), Dieterich law) and the other is the elastic coupling between the fracture and its surroundings (i.e., the load frame with a stiffness of 0.1 MPa/μm). With these parameters, the evolutions in frictional coefficient (μ), true contact-area ($R_c/R_{c,0}$), and shear strength (s/s_0) are simulated, and the results are shown in Figure 11a as bold lines. In the model, the velocity step is applied at a displacement of 0.2 mm, before which friction reaches steady state. Due to the instantaneous step in shear velocity, the true contact-area ratio decreases to $R_c = 0.957 \times R_{c,0}$, whereas the shear strength increases to $s = 1.03 \times s_0$. Although the value of $R_{c,0}$ cannot be determined uniquely, the range of $R_{c,0}$ is constrained between 0.1 and 0.3 by the R_c-k relation (Figure 9c). Thus, the reduction in R_c is estimated to be less than 0.02 (2% of the nominal fracture surface area).

With the change in R_c in mind, mechanisms that enhance the fracture permeability (k) during velocity-weakening frictional slip are discussed. In Figure 9c, experimental results on k before/after shear velocity step are shown with dotted lines. As the reduction in R_c should be limited to less than 0.02, we can discuss plausible mechanisms that change k by comparing the aperture distributions of Figure 10a with Figure 10b or those of Figure 10c with Figure 10d. Through these comparisons, it is clear that in addition to the reduction in R_c, the increase in mean aperture (i.e., dilation in the direction of normal stress, Δe_m) should occur in

satisfying the change in k, which we observe in the experiment. A conceptual model for such a mechanism is illustrated in Figure 10e. The Δe_m is 0.8 μm for the an $R_{c,0}$ value of 0.138 (Figure 10a) and is 1.4 μm for $R_{c,0}$ of 0.181 (Figure 10c). In the framework of rate- and state-dependent friction, attention is paid only to the change in the contacting asperities. However, for linking mechanical and hydraulic properties of the rock fracture, the change in mean aperture also should be considered. Such a finding can be led for the first time by coupling the laboratory experiments and the numerical modeling and is accepted as common regardless of environmental conditions. Shear-induced dilatation has been documented in fault gouge (Marone & Kilgore, 1993; Samuelson et al., 2009) and is expected to occur also for the fracture without gouge materials at the initial stage of shear. This is because the intact surface asperities are commonly damaged and gouge materials are produced during shearing (see section 3.3).

Finally, we discuss the link between stability and the permeability change in fractures. The evolution in frictional coefficient (μ), true contact-area ($R_c/R_{c,0}$), and shear strength (s/s_0) for the various conditions are explored, and Figure 11 shows the results of parametric analysis for the effects of velocity steps (Figure 11a). The a value relates to the direct effect (Figure 11b), and the b value relates to the evolution effect (Figure 11c). We prescribe the values of v_0 and D_c as common in these analyses and mainly focus on the evolution in true contact-area. As is apparent from Figure 11 that $R_c/R_{c,0}$ decreases (i.e., increase in the ratio of noncontacting asperities) with increasing shear velocity whether the rock fracture is velocity weakening (a-$b < 0$) or velocity strengthening (a-$b > 0$). The final value of $R_c/R_{c,0}$ increases with decreasing velocity step size and also with decreasing b value, whereas the final value of $R_c/R_{c,0}$ does not vary depending on a value. Considering these results, from the perspective of rate- and state-dependent friction, we can expect that fracture permeability is potentially enhanced by both stable and unstable slip. To further advance this discussion, Δe_m for the positive (a-b) values must necessarily be considered. According to Kohli and Zoback (2013), shear-induced dilation decreases with an increase in the clay and organic content but is never be less than zero. As the (a-b) value increases from negative to positive as the clay and organic content increases, we can expect that Δe_m decreases with an increase in the (a-b) value but is constantly positive. As Wang et al. (2017) pointed out, such a trend in Δe_m could be explained by considering the difference in elastic modulus. In other words, shear-induced dilation is difficult to maintain when the elastic modulus is small (e.g., clay/organic content is high). With the evolution in $R_c/R_{c,0}$ and the Δe_m, the potential relations between the stability and the permeability change are summarized as follows: Regardless of unstable slip (both velocity weakening and fast) or stable slip (velocity strengthening), the fracture permeability is enhanced once shear slip occurs. The permeability gain is possibly larger for unstable slip, since the amount of the reduction in contacting asperities and the shear-induced dilation are larger for the unstable slip. Fang et al. (2017) reported that the fracture permeability for the up-stepped velocity could be enhanced by ~10% compared to that preceding the velocity up-step, even when the (a-b) value is positive. This increase in permeability is smaller than that reported in our study (~30%), but these observations are consistent. To quantitatively analyze the role of shear-induced dilation on hydraulic properties of rock fractures, it is necessary to measure the Δe_m during the concurrent shear-flow experiments. This kind of experiment will be conducted in future work.

In summary, in this study, we propose two plausible mechanisms constraining the relationship between friction and permeability evolution. The first arises from a change in contact distribution and the second stems from shear-induced dilation triggered by the increase in shear velocity. Other mechanism such as flux-driven unclogging of the fracture possibly links frictional evolution to permeability change (Candela et al., 2015; Im et al., 2018) and will be explored. Although we cannot fully resolve which of these mechanisms dominate in a given situation, our analysis suggests that these are key processes that should be accounted for when interpreting field observation such as the abrupt permeability increase of natural faults at the onset of seismic slip (Guglielmi et al., 2015). At field scale, the role of the surface topography (roughness) on friction and permeability should be considered carefully, since roughness parameters (RMS and vertical interval) drastically increase with fracture scale (Matsuki et al., 2006; Renard et al., 2013). Future work should focus on the linkage between mechanical and hydraulic properties of field-scale fractures (the scale of tens of meters) during shear.

5. Conclusions

We evaluate the relationship between the evolution of frictional strength, stability, and fracture permeability using concurrent shear-flow experiments on a fracture in Westerly granite. Results indicate permeability

enhancement during velocity-weakening (potentially unstable) frictional slip. To explore key processes contributing to this response, we couple experimental observations with digital rock fracture modeling of aperture distribution and fluid flow. Consequently, we propose two plausible mechanisms constraining the relationship between friction and permeability evolution: (1) changes in asperity contact distribution and (2) shear-induced dilation triggered by fault slip velocity changes. Our results are fundamental in defining the impact of hydraulic stimulation and for representing the nucleation and the inhibition of seismicity (i.e., seismic cycle) adequately. By realizing the adequate hydro-mechanical coupled models of rock fractures, we will be close to the new insights into fluid migration phenomenon in response to activities in Earth's upper crust.

References

Barton, N., Bandis, S., & Bakhtar, K. (1985). Strength, deformation and conductivity coupling of rock joints. *International Journal of Rock Mechanics and Mining Sciences*, *22*(3), 121–140. https://doi.org/10.1016/0148-9062(85)93227-9

Baumberger, T., Berthoud, P., & Caroli, C. (1999). Physical analysis of the state- and rate-dependent friction law. II. Dynamic friction. *Physics Review*, *B60*, 3928–3939.

Blanpied, M. L., Lockner, D. A., & Byerlee, J. D. (1995). Frictional slip of granite at hydrothermal conditions. *Journal of Geophysical Research*, *100*(B7), 13,045–13,064. https://doi.org/10.1029/95JB00862

Blanpied, M. L., Marone, C., Lockner, D. A., Byerlee, J. D., & King, D. P. (1998). Quantitative measure of the variation in fault rheology due to fluid-rock interactions. *Journal of Geophysical Research*, *103*(B5), 9691–9712. https://doi.org/10.1029/98JB00162

Blanpied, M. L., Tullis, T. E., & Weeks, J. D. (1987). Frictional behavior of granite at low and high sliding velocities. *Geophysical Research Letters*, *14*(5), 554–557. https://doi.org/10.1029/GL014i005p00554

Brown, S. R. (1987). Fluid flow thorough rock joints: The effect of surface roughness. *Journal of Geophysical Research*, *92*(B2), 1337–1347. https://doi.org/10.1029/JB029iB02p01337

Brown, S. R., Stockman, H. W., & Reeves, S. J. (1995). Applicability of Reynolds equation for modeling fluid flow between rough surfaces. *Geophysical Research Letters*, *22*(18), 2537–2540. https://doi.org/10.1029/95GL02666

Brush, D. J., & Thomson, N. R. (2003). Fluid flow in synthetic rough-walled fractures: Navier-Stokes, Stokes, and local cubic law assumptions. *Water Resources Research*, *39*(4), 1085. https://doi.org/10.1029/2002WR001346

Candela, T., Brodsky, E. E., Marone, C., & Elsworth, D. (2015). Flow rate dictates permeability enhancement during flow pressure oscillations in laboratory experiments. *Journal of Geophysical Research: Solid Earth*, *120*, 2037–2055. https://doi.org/10.1002/2014JB011511

Chen, Z., Narayan, S. P., Yang, Z., & Rahman, S. S. (2000). An experimental investigation of hydraulic behavior of fractures and joints in granitic rock. *International Journal of Rock Mechanics and Mining Sciences*, *37*(7), 1061–1071. https://doi.org/10.1016/S1365-1609(00)00039-3

Dieterich, J. H. (1978). Time-dependent friction and the mechanics of stick slip. *Pure and Applied Geophysics*, *116*(4-5), 790–806. https://doi.org/10.1007/BF00876539

Dieterich, J. H. (1979). Modeling of rock friction 1. Experimental results and constitutive equations. *Journal of Geophysical Research*, *84*(B5), 2161–2168. https://doi.org/10.1029/JB084iB05p02161

Elkhoury, J. E., Brodsky, E. E., & Agnew, D. C. (2006). Seismic waves increase permeability. *Nature*, *441*(7097), 1135–1138. https://doi.org/10.1038/nature04798

Elkhoury, J. E., Niemeijer, A., Brodsky, E. E., & Marone, C. (2011). Laboratory observations of permeability enhancement by fluid pressure oscillation of in-situ fractured rock. *Journal of Geophysical Research*, *116*, B02311. https://doi.org/10.1029/2010JB007759

Ellsworth, W. L. (2013). Injection-induced earthquakes. *Science*, *341*, 1225942. https://doi.org/10.1126/science.1225942

Esaki, T., Du, S., Mitani, Y., Ikusada, K., & Jing, L. (1999). Development of a shear-flow test apparatus and determination of coupled properties for a single rock joint. *International Journal of Rock Mechanics and Mining Sciences*, *36*(5), 641–650. https://doi.org/10.1016/S0148-9062(99)00044-3

Evans, F. E., Genter, A., & Sausse, J. (2005). Permeability creation and damage due to massive fluid injections into granite at 3.5 km at Soultz; 1. Borehole observations. *Journal of Geophysical Research*, *110*, B04203. https://doi.org/10.1029/2004JB003168

Fang, Y., Elsworth, D., Wang, C., Ishibashi, T., & Fitts, J. P. (2017). Frictional stability-permeability relationships for fractures in shales. *Journal of Geophysical Research: Solid Earth*, *122*, 1760–1776. https://doi.org/10.1002/2016JB013435

Fang, Y., Elsworth, D., Wang, C., & Jia, Y. (2018). Mineralogical controls on frictional strength, stability, and shear permeability evolution of fracture. *Journal of Geophysical Research: Solid Earth*, *123*, 3549–3563. https://doi.org/10.1029/2017JB015338

Faoro, I., Niemeijer, A., Marone, C., & Elsworth, D. (2009). Influence of shear and deviatoric stress on the evolution of permeability in fractured rock. *Journal of Geophysical Research*, *114*, B01201. https://doi.org/10.1029/2007JB005372

Frye, K. M., & Marone, C. (2002). Effect of humidity on granular friction at room temperature. *Journal of Geophysical Research*, *107*(B11), 2309. https://doi.org/10.1029/2001JB000654

Ge, S. (1997). A governing equation for fluid flow in rock fractures. *Water Resources Research*, *33*(1), 53–61. https://doi.org/10.1029/96WR02588

Giwelli, A., Piane, C. D., Esteban, L., Clennell, M. B., Dautriat, J., Raimon, J., et al. (2016). Laboratory observations of fault transmissibility alternation in carbonate rock during direct shearing. *Geofluids*, *16*, 658–672. https://doi.org/10.1111/gfl.12183

Guglielmi, Y., Cappa, F., Avouac, J. F., Henry, P., & Elsworth, D. (2015). Seismicity triggered by fluid injection-induced aseismic slip. *Science*, *348*(6240), 1224–1226. https://doi.org/10.1126/science.aab0476

Häring, M. O., Schanz, U., Ladner, F., & Dyer, B. C. (2008). Characterisation of the Basel 1 enhanced geothermal system. *Geothermics*, *37*(5), 469–495. https://doi.org/10.1016/j.geothermics.2008.06.002

Heap, M. J., & Kennedy, B. M. (2016). Exploring the scale-dependent permeability of fractured andesite. *Earth and Planetary Science Letters*, *447*, 139–150. https://doi.org/10.1016/j.epsl.2016.05.004

Im, K., Elsworth, D., & Fang, Y. (2018). The influence of preslip sealing on the permeability evolution of fractures and faults. *Geophysical Research Letters*, *45*, 166–175. https://doi.org/10.1002/2017GL076216

Ishibashi, T., Asanuma, H., Fang, Y., Wang, C., & Elsworth, D. (2016). Exploring the link between permeability and strength evolution during shearing. In *Proceedings 50th US Rock Mechanics/Geomechanics Symposium Houston,* Texas.

Ishibashi, T., Watanabe, N., Asanuma, H., & Tsuchiya, N. (2016). Linking microearthquakes to fracture permeability change: The role of surface roughness. *Geophysical Research Letters*, *43*, 7486–7493. https://doi.org/10.1002/2016GL069478

Ishibashi, T., Watanabe, N., Hirano, N., Okamoto, A., & Tsuchiya, N. (2015). Beyond-laboratory-scale prediction for channeling flows through subsurface rock fractures with heterogeneous aperture distributions revealed by laboratory evaluation. *Journal of Geophysical Research: Solid Earth*, *120*, 106–124. https://doi.org/10.1002/2014JB01555

Jaeger, J. C., Cook, N. G. W., & Zimmerman, R. W. (2007). *Fundamentals of rock mechanics*, Malden, MA: Wiley-Blackwell.

Kang, P. K., Brown, S., & Juanes, R. (2016). Emergence of anomalous transport in stressed rough fractures. *Earth and Planetary Science Letters*, *454*, 46–54. https://doi.org/10.1016/j.epsl.2016.08.033

Kaproth, B. M., & Marone, C. (2013). Slow earthquakes, preseismic velocity changes, and the origin of slow frictional stick-slip. *Science*, *341*(6151), 1229–1232. https://doi.org/10.1126/science.1239577

Kilgore, B. D., Blanpied, M. L., & Dieterich, J. H. (1993). Velocity dependent friction of granite over a wide range of conditions. *Geophysical Research Letters*, *20*(10), 903–906. https://doi.org/10.1029/93GL00368

Kohli, A. H., & Zoback, M. D. (2013). Frictional properties of shale reservoir rocks. *Journal of Geophysical Research: Solid Earth*, *118*, 5109–5125. https://doi.org/10.1002/jgrb.50346

Kumar, S., & Bodvarsson, G. S. (1990). Fractal study and simulation of fracture roughness. *Geophysical Research Letters*, *17*(6), 701–704. https://doi.org/10.1029/GL017i006p00701

Leeman, J. R., Saffer, D. M., Scuderi, M. M., & Marone, C. (2016). Laboratory observations of slow earthquakes and the spectrum of tectonic fault slip modes. *Nature Communications*, *7*, 11104. https://doi.org/10.1038/ncomms11104

Lengliné, O., Boubacar, M., & Schmittbuhl, J. (2017). Seismicity related to the hydraulic stimulation of GRT1, Rittershoffem, France. *Geophysical Journal International*, *208*(3), 1704–1715.

Marone, C. (1998). Laboratory –derived friction laws and their application to seismic faulting. *Annual Review of Earth and Planetary Sciences*, *26*(1), 643–696. https://doi.org/10.1146/annurev.earth.26.1.643

Marone, C., & Kilgore, B. (1993). Scaling of the critical slip distance for seismic faulting with shear strain in fault zones. *Nature*, *362*(6421), 618–621. https://doi.org/10.1038/362618a0

Marone, C., Raleigh, C. B., & Scholz, C. H. (1990). Frictional behavior and constitutive modeling of simulated fault gouge. *Journal of Geophysical Research*, *95*(B5), 7007–7025. https://doi.org/10.1029/JB095iB05p07007

Matsuki, K., Chida, Y., Sakaguchi, K., & Glover, P. W. J. (2006). Size effect on aperture and permeability of a fracture as estimated in large synthetic fractures. *International Journal of Rock Mechanics and Mining Sciences*, *43*(5), 726–755. https://doi.org/10.1016/j.ijrmms.2005.12.001

McClure, M. W., & Horne, R. N. (2012). Investigation of injection-induced seismicity using a coupled fluid flow and rate/state friction model. *Geophysics*, *76*(6), 181–198.

Morrow, C. A., Bo-Chong, Z., & Byerlee, J. D. (1986). Effective pressure law for permeability of Westerly granite under cyclic loading. *Journal of Geophysical Research*, *91*(B3), 3870–3876. https://doi.org/10.1029/JB091iB03p03870

Norbeck, J. H., & Horne, R. N. (2016). Evidence for a transient hydromechanical and frictional faulting response during the 2011 M_w 5.6 Prague, Oklahoma earthquake sequence. *Journal of Geophysical Research: Solid Earth*, *121*, 8688–8705. https://doi.org/10.1002/2016JB013148

Olsson, R., & Barton, N. (2001). An improved model for hydromechanical coupling during shearing of rock joints. *International Journal of Rock Mechanics and Mining Sciences*, *38*(3), 317–329. https://doi.org/10.1016/S1365-1609(00)00079-4

Peitgen, H. O., & Saupe, D. (1988). *The science of fractal images*. New York: Springer.

Power, W. L., Tullis, T. E., & Week, J. D. (1988). Roughness and wear during brittle faulting. *Journal of Geophysical Research*, *93*(B12), 15,268–15,278. https://doi.org/10.1029/JB093iB12p15268

Pyrak-Nolte, L. J., & Nolte, D. D. (2016). Approaching a universal scaling relationship between fracture stiffness and fluid flow. *Nature Communications*, *7*, 10663. https://doi.org/10.1038/ncomms10663

Renard, F., Candela, T., & Bouchaud, E. (2013). Constant dimensionality of fault roughness from the scale of micro-fracture to the scale of continents. *Geophysical Research Letters*, *40*, 83–87. https://doi.org/10.1029/2012GL054143

Renard, F., Weiss, J., Mathiesen, J., Ben-Zion, Y., Kandula, N., & Cordonnier, B. (2018). Critical evolution of damage toward system-size failure in crystalline rock. *Journal of Geophysical Research: Solid Earth*, *123*, 1969–1986. https://doi.org/10.1002/2017JB014964

Rice, J. R., & Ruina, A. L. (1983). Stability of steady frictional slipping. *Journal of Applied Mechanics*, *80*, 343–349.

Ruina, A. (1983). Slip instability and state variable friction laws. *Journal of Geophysical Research*, *88*(B12), 10,359–10,370. https://doi.org/10.1029/JB088iB12p10359

Samuelson, J., Elsworth, D., & Marone, C. (2009). Shear-induced dilatancy of fluid-saturated faults: Experiment and theory. *Journal of Geophysical Research*, *114*, B12404. https://doi.org/10.1029/2008JB006273

Scholz, C. (1987). Wear and gouge formation in brittle faulting. *Geology*, *15*(6), 493–495. https://doi.org/10.1130/0091-7613(1987)15<493:WAGFIB>2.0.CO;2

Scholz, C. (2002). *The mechanics of earthquakes and faulting* (2nd ed.). Cambridge, UK: Cambridge University Press. https://doi.org/10.1017/CBO9780511818516

Scuderi, M. M., & Collettini, C. (2016). The role of fluid pressure in induced vs. triggered seismicity: Insights from rock deformation experiments on carbonates. *Scientific Reports*, *6*(1), 24852. https://doi.org/10.1038/srep24852

Trimmer, D., Bonner, B., Heard, H. C., & Duba, A. (1980). Effect of pressure and stress on water transport in intact and fractured gabbro and granite. *Journal of Geophysical Research*, *85*(B12), 7059–7071. https://doi.org/10.1029/JB085iB12p07059

Tsang, Y. W., & Witherspoon, P. A. (1981). Hydromechanical behavior of a deformable rock fracture subject to normal stress. *Journal of Geophysical Research*, *86*(B10), 9287–9298. https://doi.org/10.1029/JB086iB10p09287

Wang, C., Elsworth, D., & Fang, Y. (2017). Influence of weakening minerals on ensemble strength and slip stability of faults. *Journal of Geophysical Research: Solid Earth*, *122*, 7090–7110. https://doi.org/10.1002/2016JB013687

Wang, W., & Scholz, C. H. (1994). Wear processes during frictional sliding of rock: A theoretical and experimental study. *Journal of Geophysical Research*, *99*(B4), 6789–6799. https://doi.org/10.1029/93JB02875

Watanabe, N., Hirano, N., & Tsuchiya, N. (2009). Diversity of channeling flow in heterogeneous aperture distribution inferred from integrated experimental-numerical analysis on flow through shear fracture in granite. *Journal of Geophysical Research*, *114*, B04208. https://doi.org/10.1029/2008JB005959

Witherspoon, P. A., Wang, J. S. Y., Iwai, K., & Gale, J. E. (1980). Validity of cubic law for fluid flow in a deformable rock fracture. *Water Resources Research*, *16*(6), 1016–1024. https://doi.org/10.1029/WR016i006p01016

Xue, L., Li, H.-B., Brodsky, E. E., Xu, Z.-Q., Kano, Y., Wang, H., et al. (2013). Continuous permeability measurements record healing inside the Wenchuan earthquake fault zone. *Science*, *340*(6140), 1555–1559. https://doi.org/10.1126/science.1237237